AIAA JOURNAL
Vol. 48, No. 9, September 2010

Optimizing a Boundary-Layer-Ingestion Offset Inlet by Discrete Adjoint Approach

Byung Joon Lee* and Meng-Sing Liou†
NASA John H. Glenn Research Center at Lewis Field, Cleveland, Ohio 44135
and
Chongam Kim‡
Seoul National University, Seoul 151-742, Republic of Korea

DOI: 10.2514/1.J050222

A large amount of low-momentum boundary-layer flow ingesting into a flush-mounted inlet can cause significant total pressure loss and distortion to the extent beyond operability of a fan/compressor. To improve the quality of incoming flow into the engine, shape optimization of the surface geometry at the inlet entrance has been carried out using the discrete adjoint method; the inlet-floor shape is parameterized by the use of control points on B-spline surface patches. To resolve the complicated geometry flexibly and wall-bounded turbulent flow accurately, an overset mesh system is well-suited for integrating the flow analysis code, sensitivity analysis code, and grid modification tools. To enhance the convergence characteristics of the sensitivity analysis code, additional numerical dissipation for the discrete adjoint formulation is introduced. After using this optimization procedure, the new inlet yields a significant improvement in performance: a more than 50% reduction in flow distortion and a 3% increase in total pressure recovery. High performance at off-design conditions is also realized with only slight degradation, confirming the capability of the adjoint method for a practical design problem. Finally, the physical meaning and implication of the performance improvement are elaborated upon in relation to the flow characteristics resulting from the new design .

Nomenclature

A_c	=	captured area
A_i	=	inlet throat area
A_0	=	inlet mass flow stream-tube area at freestream condition
A_2	=	area of AIP
AIP	=	aerodynamic interface plane between the inlet and the engine fan face
b	=	distance from throat station to inlet highlight
CR	=	contraction ratio ($=A_i/A_2$)
DPCP	=	Society of Automotive Engineers circumferential distortion descriptor, Eq. (32)
D_2	=	diameter of AIP
H_i	=	height of inlet throat
L	=	length from inlet throat station to AIP
M_2	=	Mach number at AIP
M_∞	=	freestream Mach number
MFP	=	mass flux (flow) parameter, Eqs. (1) and (2)
MFR	=	mass flux (flow) ratio ($=A_0/A_c = (\rho u)_c/(\rho u)_0$)
γ	=	ratio of specific heats of air
η	=	total pressure recovery of the duct, Eq. (31)

I. Introduction

RECENTLY, interest in hybrid wing/body (HWB) configuration has intensified, as represented in several design and test studies [1–3]. Unlike the conventional commercial aircraft, the HWB has engine mounted on the top side of airframe; active interest in this concept by NASA began in early 2000s because of its promising advantages in reducing ram drag, structural weight, and wetted area [2,3]. Moreover, as engines are installed in the rear end, also in proximity to or embedded in the fuselage, the boundary layer developed along the aircraft top surface is ingested into the inlet of the engine. Thus, the inlet is called boundary-layer ingesting (BLI) inlet. A major issue of the BLI inlet is how the deteriorated incoming flow caused by boundary-layer ingestion can be managed. The height of ingested boundary layer can reach as high as 30% of inlet height [1–3]. In addition, an S-curved diffuser, being geometrically necessary for accommodating the misalignment in elevations of inlet entrance and engine, can negatively affect inlet efficiency and flow distortion at the engine fan face, because of secondary and separated flows. In addition, a large separation at the juncture of lip and bottom surface can significantly increase total pressure loss. Thus, the boundary-layer ingestion and the cowl-lip separation together with the separation generated by S-curved surface make the design of BLI inlet more difficult than a conventional S-shaped inlet.

In previous studies, distortion reduction of an S-shaped inlet has been sought by using passive or active control concepts actively. Most passive control ideas employed devices such as vortex generating vanes (VGs) and Gaussian bump [4–11]. Taylor [4] devised a vortex generator to reenergize the boundary layer to prevent flow separation and applied it to inlet flow control. But it did not work well in three-dimensional geometries because their design work is based on two-dimensional boundary-layer concepts. Kaldschmidt et al. [5] demonstrated that VGs, used to alter the direction of secondary flow, could reduce engine fan face distortion effectively. Based on the previous researches for the effects of VGs, Anderson and Gibb [7] carried out a computational fluid dynamics (CFD) analysis to investigate the performance of an S-duct with VGs. The Gaussian bump devised by Zhang et al. [8] is another device to manage the distortion by changing the swirling direction of flow separation. However, VGs seems to be preferred by many researchers in their computational and experimental studies [7,9,12–16]. A recent attempt by Jirasek [9] showed that flow distortion in an offset inlet could be effectively decreased via elimination of flow separation by optimizing vane size and location of VGs. It is also clear that there is still room for improvement in terms of design methodology

Presented as Paper 2009-3804 at the 19th AIAA Computational Fluid Dynamics Conference, San Antonio, TX, 22–25 June 2009; received 16 September 2009; revision received 20 January 2010; accepted for publication 31 January 2010.

*NASA Postdoctoral Program Fellow. Member AIAA.
†Senior Technologist, Aeropropulsion Division. Associate Fellow AIAA.
‡Professor, School of Mechanical and Aerospace Engineering. Member AIAA.

because the metamodel used in [9] is only reliable with a few design variables, thus preventing the design process from exploring a sufficiently extended design space.

Designs of duct shapes to diminish the size of flow separation have been performed in [10,11], in which a large number of design variables were included in the adjoint-based sensitivity analysis. Lim and Choi [10] eliminated flow separation in a two-dimensional S-shaped duct. Lee and Kim [11] reduced the total pressure loss by using NURBS function in a three-dimensional problem and demonstrated that the designed geometry could also have good performance at off-design conditions. The resulting geometry is rather difficult to be realized at the manufacturing stage.

As for inlets with large BLI, there has been very little study on flow control and design optimization. Anabtawi et al. [12] experimentally studied passive flow control for a BLI offset inlet at very low Mach number condition. Gorton et al. [13] conducted experiments to investigate the performance of active flow control by jets and passive control by VGs. Berrier and Allan [14] validated the use of OVERFLOW code for transonic BLI inlet with flow control, by comparing computational and experimental results. Based on the validation, Allan et al. [15,16] carried out the optimal design of active and passive control devices to minimize distortion and high-cycle fatigue, based on methods of overset mesh and design of experiment (DOE). From these experimental and CFD studies, it is evident that the inlet distortion can be managed for flow having boundary-layer thickness of 30% channel height, by way of flow control devices such as VGs or blowing jets. These flow control devices for offset inlet are mostly designed by using parametric studies or DOE via surrogate models; these approaches, however, are reliable only for a few design parameters. Furthermore, even though VGs can reduce distortion effectively, they alone may not improve the inlet efficiency, due to other complexities such as flow separation at cowl lip. To manage this lip separation, new design concepts besides VGs should be considered as well.

In the present work, an adjoint-based approach is applied to design the BLI inlet and is combined with an overset mesh technique. A large number of design variables (about 500) are used to represent changes in surface geometry over an extended design space and in a general manner so as to effectively produce improvement in BLI inlet performance. We shall describe in this paper the adjoint formulation for the overset mesh system and the numerical dissipation added to improve the convergence in sensitivity analysis. Significant improvement in performance characteristics is demonstrated for both design and off-design conditions.

II. Flow Analysis and Validation

A. Baseline Geometry and Mesh System

The Boeing Company, under a contract with NASA, designed four BLI S-duct inlets to fit in the design space of a large HWB transport configuration as well as smaller military-fighter-type applications with flush-mounted inlets [17]. Among the geometries considered, a circular-type BLI inlet (type A in [17]) is used in the present work for the demonstration of our design approach. The overset mesh system for the BLI inlet is shown in Fig. 1. The diameter of aerodynamic interface plane (AIP) D_2 is 2.448 in., and the ratio of AIP area A_2 to inlet throat area A_i is 1.070. The length L from inlet throat station to AIP is 7.697 in., and the distance b from throat station to inlet highlight is 0.477 in. The height of inlet throat H_i is 1.703 in. and the captured area A_c is 5.760 in.^{2}. Here, the subscript *0* denotes far upstream or freestream, *2* represents AIP of engine, *c* is at inlet lip, and *i* is throat station. The overset mesh system of the inlet geometry consists of 10 blocks, with 5 configuration blocks representing the domains around the inlet and 5 background blocks for the external boundary conditions. In Fig. 1, the surface grids are presented describing the entrance region of the present geometry, where four configuration blocks and one background block are shown as an example. The entire mesh for the baseline inlet has 4.5 million grid points. The computation domain extends from $x/D_2 = -20.0$ to $x/D_2 = 20.0$ in the streamline direction. The boundary conditions imposed at both planes are described in the next section.

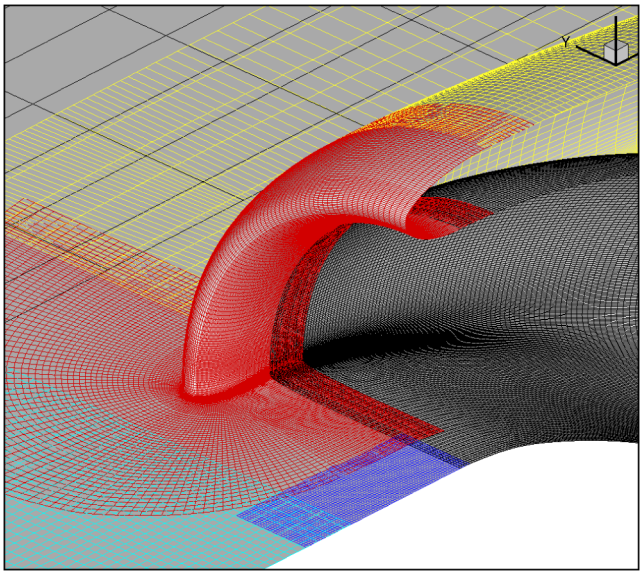

Fig. 1 Overset mesh system for BLI inlet (for clarity, only some grid blocks are shown).

B. Boundary Conditions

A boundary layer with a thickness that is 30% of the height of inlet highlight has been generated in the inflow having freestream Mach number of 0.85 and Reynolds number of 3.8 million based on the diameter of AIP D_2. The profile of the inflow boundary layer is obtained by solving a turbulent flat-plate flow problem. The pressure at outflow is set by matching the static pressure that meets the required mass flow rate for the engine operating condition [18]. The equations for determining the static pressure condition are given by Eqs. (1–3), through the use of nondimensional mass flow rate in term of mass flow parameter (MFP), which is defined for isentropic flow at freestream condition as

$$\mathrm{MFP}_{\infty} = \sqrt{\gamma} M_{\infty} \left(1 + \frac{\gamma - 1}{2} M_{\infty}^2\right)^{-\frac{1}{2}\frac{\gamma+1}{\gamma-1}} \tag{1}$$

The MFP at engine fan face can be evaluated similarly, but by using Mach number at AIP M_2:

$$\mathrm{MFP}_2 = \sqrt{\gamma} M_2 \left(1 + \frac{\gamma - 1}{2} M_2^2\right)^{-\frac{1}{2}\frac{\gamma+1}{\gamma-1}} = \frac{\mathrm{MFP}_{\infty} \cdot \mathrm{MFR} \cdot \mathrm{CR}}{\eta} \tag{2}$$

The contraction ratio (CR) of the test geometry is $A_2/A_i = 0.9346$. The estimated total pressure recovery and MFR are given according to the experimental data for each test condition [19]. By solving Eq. (2) via Newton–Raphson method, Mach number at AIP M_2 can be obtained.

The ratio of static back pressure to freestream pressure is then determined by

$$\frac{p_2}{p_{\infty}} = \eta \frac{(1 + \frac{\gamma-1}{2} M_{\infty}^2)^{\frac{\gamma}{\gamma-1}}}{(1 + \frac{\gamma-1}{2} M_2^2)^{\frac{\gamma}{\gamma-1}}} \tag{3}$$

C. Numerical Schemes

Three-dimensional Reynolds-averaged Navier–Stokes (RANS) equations are used with the *k-w* SST model, which has been found to provide good accuracy for duct analysis [20]. A modified Roe scheme RoeM [21] is used for evaluating the inviscid fluxes. For higher-order spatial accuracy, MUSCL interpolation is used with the minmod limiter and LU-SGS [22] is chosen for time integration.

D. Flow Analysis and Validation

Berrier and Allan [14] carried out CFD computation using OVERFLOW and compared the numerical results with experimental data [19]. The experiment was performed at Reynolds number of

3.8 million, but the CFD results at Reynolds number of 2.2 million were used for comparison. In the present work, we compared the results of both conditions. Figure 2 shows the boundary-layer profiles at the locations of $x = 0.10$ and $y = 1.7$ in. upstream of cowl lip. The height of ingested boundary layer is about 35% of the height of inlet highlight. Figure 3 shows the static pressure distributions. As in [14], our predicted pressure distribution for $Re = 2.2 \times 10^6$ shows a better agreement with the data. However, the mass flux ratio A_0/A_c,[§] total pressure recovery, and DPCP all show larger discrepancies than those of $Re = 3.8 \times 10^6$. Relevant performance factors for both cases are presented in Table 1. Figure 4 shows the comparison of total pressure contours at AIP with the CFD and experimental results by Allan et al.; it is evident that the contours of $Re = 3.8 \times 10^6$ are closer to the experimental data than the $Re = 2.2 \times 10^6$ contour from the current study and also from the results of [14]. Also, results of $Re = 2.2 \times 10^6$ from the present work and [14] show that the height of low total pressure region is taller than the experimental data. Because of these observations, all of the CFD comparisons and design results from the current study are made at $Re = 3.8 \times 10^6$ hereafter. Figure 5 shows streamlines at the entrance of inlet, revealing flow separations at two locations, one on the inlet floor and the other on the internal cowl surface. These separation bubbles should be reduced in order to increase the performance of BLI inlet; in this paper, we shall employ a design optimization strategy to significantly reduce the flow separation on the inlet floor.

III. Design Optimization

A. Sensitivity Analysis 1: Discrete Adjoint Method

For sensitivity analysis, we employ a discrete adjoint solver, which is developed by hand-differentiation of the flow solver described above; the details can be found in [23–25]. For the case when a huge number of design variables are required, such as the present design of duct shape, the adjoint method is efficient because the time cost of sensitivity analysis is almost independent of the number of design variables.

The discrete residual vector $\mathbf{R}$ ($m \times 1$ column vector, $m = 7$ in our case of using a two-equation turbulence model) of the steady-state governing equations can be expressed as a function of flow variable vector $\mathbf{Q}$ ($m \times 1$), grid position vector $\mathbf{X}$ (3×1), and a vector of design variables $\mathbf{D}$ ($n \times 1$, $n \gg 1$ in our case):

$$\mathbf{R} = \mathbf{R}(\mathbf{Q}, \mathbf{X}, \mathbf{D}) = \mathbf{0} \tag{4}$$

The objective function f to be maximized or minimized is dependent on $\mathbf{Q}$, $\mathbf{X}$, and $\mathbf{D}$:

$$f = f(\mathbf{Q}, \mathbf{X}, \mathbf{D}) \tag{5}$$

The sensitivity derivatives of the objective function with respect to the design variable $\mathbf{D}$ is obtained by the chain-rule differentiation:

$$\frac{\mathrm{d}f}{\mathrm{d}\mathbf{D}} = \frac{\partial f}{\partial \mathbf{Q}}\frac{\mathrm{d}\mathbf{Q}}{\mathrm{d}\mathbf{D}} + \frac{\partial f}{\partial \mathbf{X}}\frac{\mathrm{d}\mathbf{X}}{\mathrm{d}\mathbf{D}} + \frac{\partial f}{\partial \mathbf{D}} \tag{6}$$

The sensitivity values can be evaluated by solving Eq. (6) with time-iterative method. However, the term $\mathrm{d}\mathbf{Q}/\mathrm{d}\mathbf{D}$ can increase the computation cost as the number of design variables increases. Thus, the term can be eliminated by adopting adjoint variables. The discrete residual is then differentiated with respect to design variables to yield a $m \times n$ Jacobian matrix:

$$\frac{\mathrm{d}\mathbf{R}}{\mathrm{d}\mathbf{D}} = \frac{\partial \mathbf{R}}{\partial \mathbf{Q}}\frac{\mathrm{d}\mathbf{Q}}{\mathrm{d}\mathbf{D}} + \frac{\partial \mathbf{R}}{\partial \mathbf{X}}\frac{\mathrm{d}\mathbf{X}}{\mathrm{d}\mathbf{D}} + \frac{\partial \mathbf{R}}{\partial \mathbf{D}} = \mathbf{0} \tag{7}$$

[§]The area ratio characterizes an equivalent one-dimensional stream-tube in which A_0 is the area that can supply freestream flow with the specified mass flow rate to the inlet of area A_c at highlight. From the continuity equation $A_0/A_c = (\rho u)_c/(\rho u)_0$, it is also the ratio of mass fluxes at these two stations, denoted as MFR, but sometimes referred to as the mass flow ratio in the literature.

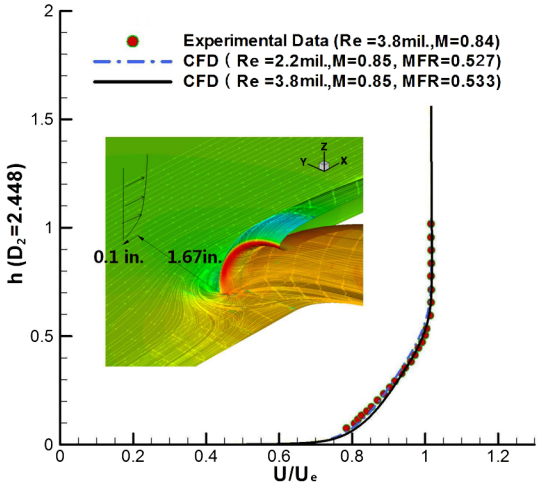

Fig. 2 Comparison of boundary-layer profiles of incoming flow at two different Reynolds numbers to the experiment [19].

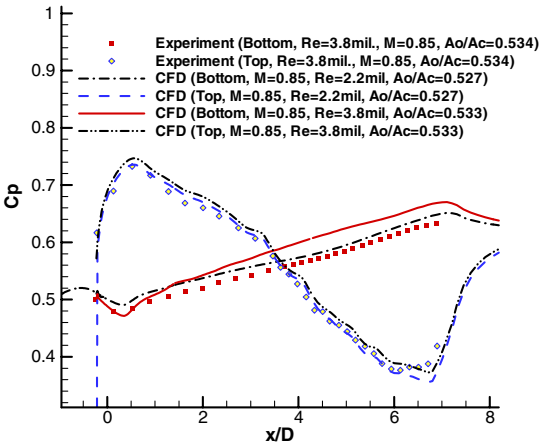

Fig. 3 Comparison of pressure distributions with experiment [19] along the longitudinal direction.

Equations (6) and (7) are then combined by using an adjoint vector $\mathbf{\Lambda}$ ($m \times 1$), which has the dimension of the residual $\mathbf{R}$:

$$\frac{\mathrm{d}f}{\mathrm{d}\mathbf{D}} = \frac{\partial f}{\partial \mathbf{Q}}\frac{\mathrm{d}\mathbf{Q}}{\mathrm{d}\mathbf{D}} + \frac{\partial f}{\partial \mathbf{X}}\frac{\mathrm{d}\mathbf{X}}{\mathrm{d}\mathbf{D}} + \frac{\partial f}{\partial \mathbf{D}} + \mathbf{\Lambda}^T\left(\frac{\partial \mathbf{R}}{\partial \mathbf{Q}}\frac{\mathrm{d}\mathbf{Q}}{\mathrm{d}\mathbf{D}} + \frac{\partial \mathbf{R}}{\partial \mathbf{X}}\frac{\mathrm{d}\mathbf{X}}{\mathrm{d}\mathbf{D}} + \frac{\partial \mathbf{R}}{\partial \mathbf{D}}\right) \tag{8}$$

Equation (8) can be rearranged by grouping the $\mathrm{d}\mathbf{Q}/\mathrm{d}\mathbf{D}$ term:

$$\frac{\mathrm{d}f}{\mathrm{d}\mathbf{D}} = \frac{\partial f}{\partial \mathbf{X}}\left\{\frac{\mathrm{d}\mathbf{X}}{\mathrm{d}\mathbf{D}}\right\} + \frac{\partial f}{\partial \mathbf{D}} + \mathbf{\Lambda}^T\left(\frac{\partial \mathbf{R}}{\partial \mathbf{X}}\frac{\mathrm{d}\mathbf{X}}{\mathrm{d}\mathbf{D}} + \frac{\partial \mathbf{R}}{\partial \mathbf{D}}\right) + \left(\frac{\partial f}{\partial \mathbf{Q}} + \mathbf{\Lambda}^T\frac{\partial \mathbf{R}}{\partial \mathbf{Q}}\right)\frac{\mathrm{d}\mathbf{Q}}{\mathrm{d}\mathbf{D}} \tag{9}$$

Without evaluating the matrix $\mathrm{d}\mathbf{Q}/\mathrm{d}\mathbf{D}$, the sensitivity derivatives can be greatly simplified to

$$\frac{\mathrm{d}f}{\mathrm{d}\mathbf{D}} = \frac{\partial f}{\partial \mathbf{X}}\frac{\mathrm{d}\mathbf{X}}{\mathrm{d}\mathbf{D}} + \frac{\partial f}{\partial \mathbf{D}} + \mathbf{\Lambda}^T\left(\frac{\partial \mathbf{R}}{\partial \mathbf{X}}\frac{\mathrm{d}\mathbf{X}}{\mathrm{d}\mathbf{D}} + \frac{\partial \mathbf{R}}{\partial \mathbf{D}}\right) \tag{10}$$

provided the adjoint vector $\mathbf{\Lambda}$ satisfies the following adjoint equation:

$$\frac{\partial f}{\partial \mathbf{Q}} + \mathbf{\Lambda}^T\frac{\partial \mathbf{R}}{\partial \mathbf{Q}} = \mathbf{0} \tag{11}$$

Table 1 Comparison of performance coefficients according to Reynolds number

Reynolds number	Total pressure recovery	Distortion	Mass flow ratio A_0/A_c
3.8 mil. Exp [18]	0.952	0.0540	0.534
3.8 mil. CFD (current study)	0.956	0.0596	0.533
2.2 mil. CFD (current study)	0.943	0.0630	0. 527

The solution vector $\mathbf{\Lambda}$ is then obtained in a time-iterative manner. In the present paper, this is done by the Euler-implicit linearization of Eq. (11):

$$\left[\frac{\mathbf{I}}{J\Delta t}+\left(\frac{\partial \mathbf{R}}{\partial \mathbf{Q}}\right)^T\right]\Delta\mathbf{\Lambda}=-\left(\frac{\partial \mathbf{R}}{\partial \mathbf{Q}}\right)^T\mathbf{\Lambda}^m-\left(\frac{\partial f}{\partial \mathbf{Q}}\right)^T \tag{12}$$

And the vector $\mathbf{\Lambda}$ is updated by

$$\mathbf{\Lambda}^{m+1}=\mathbf{\Lambda}^m+\Delta\mathbf{\Lambda} \tag{13}$$

until a preset convergence criterion is satisfied.

B. Sensitivity Analysis 2: Boundary Conditions for the Overset Block Interface

Adjoint formulation on the overset boundary can be derived similarly, by slightly modifying the conventional discrete adjoint boundary conditions. The boundary conditions can be expressed as

$$\left(\frac{\partial \mathbf{R}^M}{\partial \mathbf{Q}^M}\right)^T\mathbf{\Lambda}^M+\left(\frac{\partial \mathbf{R}_F^S}{\partial \mathbf{Q}^M}\right)^T\mathbf{\Lambda}_F^S+\left(\frac{\partial f^M}{\partial \mathbf{Q}^M}\right)^T=\mathbf{0} \tag{14}$$

$$\left(\frac{\partial \mathbf{R}^S}{\partial \mathbf{Q}^S}\right)^T\mathbf{\Lambda}^S+\left(\frac{\partial \mathbf{R}_F^M}{\partial \mathbf{Q}^S}\right)^T\mathbf{\Lambda}_F^M+\left(\frac{\partial f^S}{\partial \mathbf{Q}^S}\right)^T=\mathbf{0} \tag{15}$$

$$\left(\frac{\partial \mathbf{R}^M}{\partial \mathbf{Q}_F^M}\right)^T\mathbf{\Lambda}^M+\left(\frac{\partial \mathbf{R}_F^M}{\partial \mathbf{Q}_F^M}\right)^T\mathbf{\Lambda}_F^M+\left(\frac{\partial f^M}{\partial \mathbf{Q}_F^M}\right)^T=\mathbf{0} \tag{16}$$

$$\left(\frac{\partial \mathbf{R}^S}{\partial \mathbf{Q}_F^S}\right)^T\mathbf{\Lambda}^S+\left(\frac{\partial \mathbf{R}_F^S}{\partial \mathbf{Q}_F^S}\right)^T\mathbf{\Lambda}_F^S+\left(\frac{\partial f^S}{\partial \mathbf{Q}_F^S}\right)^T=\mathbf{0} \tag{17}$$

where the subscript F indicates a fringe cell. The superscripts M and S denote the main-grid and subgrid domains, respectively. By solving the four equations sequentially, the overset boundary values on the main- and subgrids can be updated. For the subgrid domain, the fringe cell value of the main grid $\mathbf{\Lambda}_F^M$ is firstly updated from the interior cell value of the main grid $\mathbf{\Lambda}^M$ using Eq. (16). The interior cell value of the subgrid $\mathbf{\Lambda}^S$ is then updated from the fringe cell value of the main grid $\mathbf{\Lambda}_F^M$ as in Eq. (15). For the main-grid domain, Eqs. (14) and (17) are used in a similar manner. The fringe cell value of the subgrid $\mathbf{\Lambda}_F^S$ is updated from the interior cell value of the subgrid $\mathbf{\Lambda}^S$ using Eq. (17). The interior cell value of the main grid $\mathbf{\Lambda}^M$ is finally updated from the fringe cell value of the subgrid $\mathbf{\Lambda}_F^M$ from Eq. (14). The updating procedure of the adjoint variables on the overset boundary is simply reverse to that of the flow variables because of the transposed operation in the adjoint formulation.

C. Sensitivity Analysis 3: Numerical Dissipation

To ensure stable convergence, we propose to add a fourth-order numerical dissipation to the discrete adjoint formulation. To describe how the dissipation term is added to enhance diagonal dominance in the first term of the right-hand side (RHS) in Eq. (12), let us consider a one-dimensional problem and use a variable $\mathbf{G}$ for brevity:

$$\mathbf{G}_i=\left(\frac{\partial \mathbf{R}_i}{\partial \mathbf{Q}_i}\right)^T\cdot\mathbf{\Lambda}_i \tag{18}$$

Then, the dissipation term $\mathrm{d}/\mathrm{d}x\,(\varepsilon \mathrm{d}^3\mathbf{G}/\mathrm{d}x^3)\,\Delta x^4$ distributed on a five-point stencil, which is used for third-order spatial accuracy, gives the following discrete form:

$$\begin{aligned}\mathbf{SD}_i=&\varepsilon_{i+1/2}\mathbf{G}_{i+2}-(3\varepsilon_{i+1/2}+\varepsilon_{i-1/2})\mathbf{G}_{i+1}+(3\varepsilon_{i+1/2}+3\varepsilon_{i-1/2})\mathbf{G}_i\\&-(\varepsilon_{i+1/2}+3\varepsilon_{i-1/2})\mathbf{G}_{i-1}+\varepsilon_{i-1/2}\mathbf{G}_{i-2}\end{aligned} \tag{19}$$

where $0\le\varepsilon_{i+1/2}\ll 1$ is an adjustable dissipation coefficient at the cell interface and is detailed below.

After adding the above dissipation term to the RHS of the adjoint equation, Eq. (12), we have

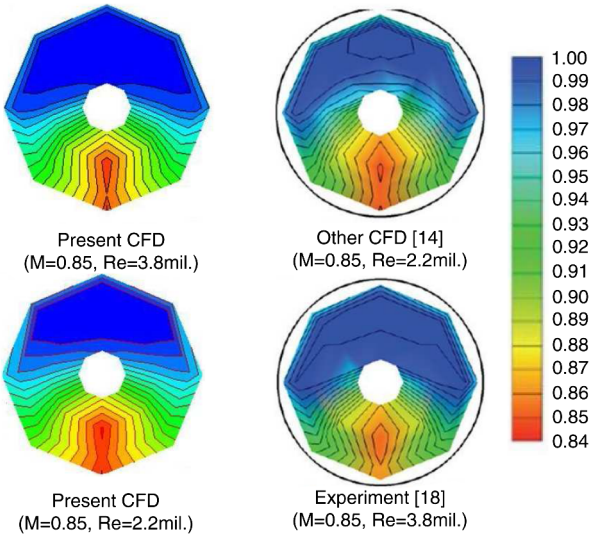

Fig. 4 Comparison of total pressure contours at AIP.

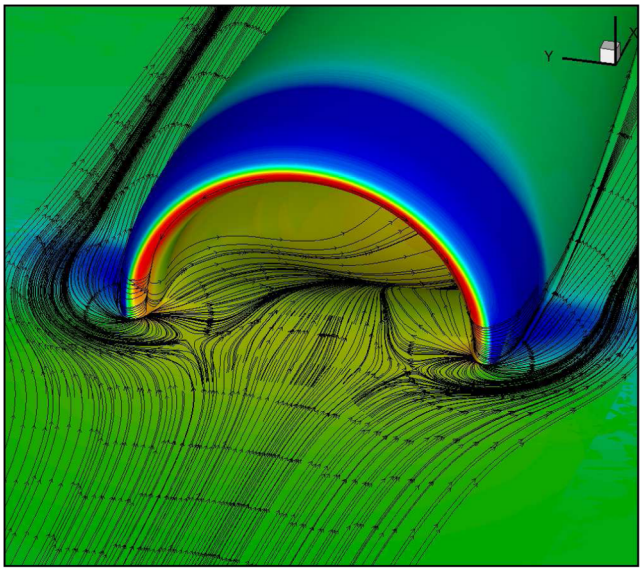

Fig. 5 Oil flow patterns by CFD at the entrance of the baseline BLI inlet.

$$\begin{aligned}\mathbf{RHS}_i - \mathbf{SD}_i = &-\left[\left(1+\varepsilon_{i+\frac{1}{2}}\right)\left(\frac{\partial \mathbf{R}_{i+2}}{\partial \mathbf{Q}_i}\right)^T\right]\mathbf{\Lambda}^m_{i+2}\\ &-\left[\left(1-3\varepsilon_{i+\frac{1}{2}}-\varepsilon_{i-\frac{1}{2}}\right)\left(\frac{\partial \mathbf{R}_{i+1}}{\partial \mathbf{Q}_i}\right)^T\right]\mathbf{\Lambda}^m_{i+1}\\ &-\left[\left(1+3\varepsilon_{i+\frac{1}{2}}+3\varepsilon_{i-\frac{1}{2}}\right)\left(\frac{\partial \mathbf{R}_{i}}{\partial \mathbf{Q}_i}\right)^T\right]\mathbf{\Lambda}^m_{i}\\ &-\left[\left(1-\varepsilon_{i+\frac{1}{2}}-3\varepsilon_{i-\frac{1}{2}}\right)\left(\frac{\partial \mathbf{R}_{i-1}}{\partial \mathbf{Q}_i}\right)^T\right]\mathbf{\Lambda}^m_{i-1}\\ &-\left[\left(1+\varepsilon_{i-\frac{1}{2}}\right)\left(\frac{\partial \mathbf{R}_{i-2}}{\partial \mathbf{Q}_i}\right)^T\right]\mathbf{\Lambda}^m_{i-2} \qquad (20)\end{aligned}$$

The dissipation coefficient requires further clarification. It is basically scaled by the spectral radius of the flux Jacobian, and takes into account different magnitudes in the case of multidimensional problems. Hence, the dissipative term can be written as a product of a function of spectral radii and a scaling coefficient:

$$\varepsilon_{i+1/2} = \varepsilon^{(4)} C_{i+1/2}, \quad \text{and} \quad C_{i+1/2} = \frac{1}{2}[C_{\xi_{i+1}} + C_{\xi_i}] \qquad (21)$$

where

$$C_\xi = e_\xi \varphi_\xi, \qquad \varphi_\xi = \sqrt{1+(e_\eta/e_\xi)^\sigma}, \qquad \sigma = 2/3 \ \text{(2-D case)} \qquad (22)$$

and e is the spectral radius of the flux Jacobian matrices in the body-fitted curvilinear directions that conform to the body surface. A conservative estimate of this spectral radius is given according to the following formula:

$$e = u \cdot \hat{n} + a\sqrt{n_x^2 + n_y^2} \qquad (23)$$

where a is the speed of sound at the cell center and n is the area vectors at the face in the ξ direction. The fourth-order coefficient is determined via a second-order difference (smoothness) function ν:

$$\varepsilon^{(4)} = \max(0, (k^{(4)} - \varepsilon^{(2)})), \qquad \varepsilon^{(2)} = k^{(2)} \max(\nu_{i,j}, \nu_{i+1,j}) \qquad (24)$$

where

$$\nu_{i,j} = \frac{|P_{t_{i+1,j}} - 2P_{t_{i,j}} + P_{t_{i-1,j}}|}{|P_{t_{i+1,j}} + 2P_{t_{i,j}} + P_{t_{i-1,j}}|} \qquad (25)$$

and $P_{t_{i,j}}$ is the total pressure at cell (i, j).

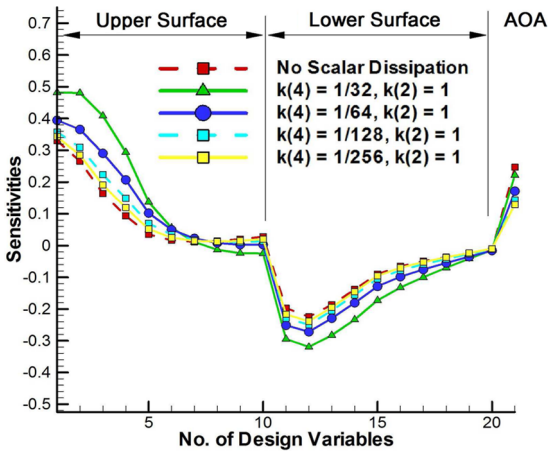

Fig. 6 Effects of artificial damping coefficient on the sensitivities of drag coefficient with respect to design variables for NACA0012 airfoil. Design variables are based on Hicks–Henne functions [28]; there are 10 variables on the upper surface and 10 on the lower surface.

As shown in Eq. (20), the diagonal terms becomes more dominant by considering the ratio of diagonal term to the sum of off-diagonal terms, where a slight increase in the off-diagonal terms at $(i-2)$ and $(i+2)$ is compensated by the decrease in terms at $(i-1)$ and $(i+1)$.

To prevent deterioration of accuracy caused by the dissipation term, the coefficient $\varepsilon^{(2)}$ is taken proportional to the normalized second difference of total pressure, which acts as a sensor that turns off the dissipation near the region having high total pressure variation near the separation as well as the shock waves.

To quantify an adequate amount of dissipation, sensitivity functions resulting from various values of $k^{(4)}$ are compared in Fig. 6 against the case of no dissipation added for a transonic airfoil problem; $k^{(4)} = 1/128$ gives reasonable accuracy, while improving convergence (not shown). Hence, the sensitivity analysis and design are performed with $k^{(4)} = 1/128$ and $k^{(2)} = 1$ hereafter. It is noted that the determination of these coefficients is still problem-dependent. As the dissipation increases, the adjoint Jacobian matrix becomes more diagonal dominant, but the accuracy of gradients decreases. In Fig. 7, the residual histories of three-dimensional flow and sensitivity calculations for the BLI inlet are presented for overset blocks. The flow solver shows relatively poor convergence in some blocks such as lip and cover blocks, where the external shock wave or lip separation is observed. On the other hand, the convergence in the duct block where the performance coefficients are evaluated is quite good. Thus, in Fig. 8 we see that the performance coefficients continue to converge towards an asymptotic value after flow residuals having reduced by about four orders of magnitude.

D. Design Parameters

As mentioned before, the design of BLI inlet is different from other S-shaped inlets because the boundary layer from the configuration

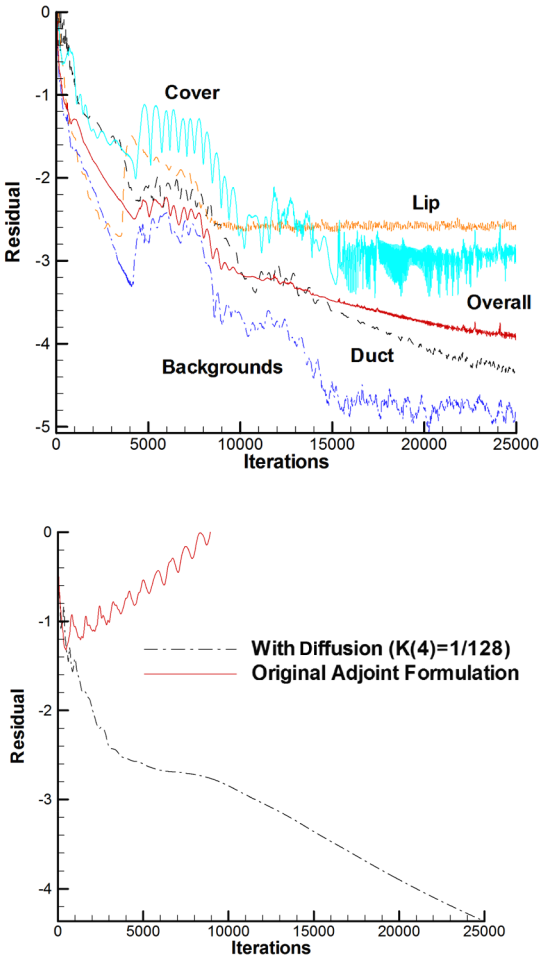

Fig. 7 Residual histories for BLI inlet.

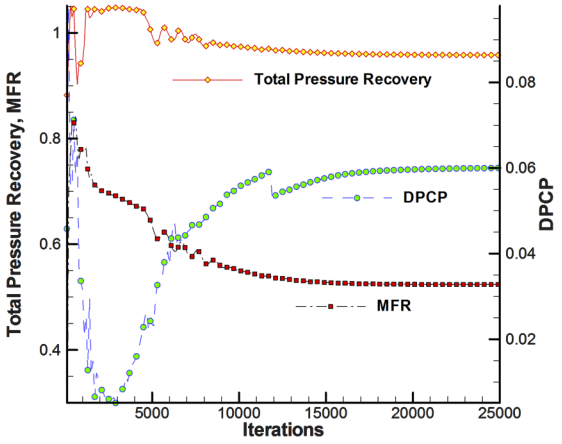

Fig. 8 History of performance coefficients (CFL = 3.0).

surface is ingested directly in the case of BLI inlet. Therefore, flow distortion due to the boundary layer should be considered as important as the secondary flow generated by the S-curved duct geometry itself. In the present work, a B-spline function, constructed as a spline patch of the baseline surface mesh, is used as geometric parameters. Then, the surface meshes can be modified by adjusting the position of the control points. The coordinate vector of the surface, $\mathbf{X}(u, v)$ in the parameter space, is expressed in terms of the position vector $\boldsymbol{P}_{i,j} = (x_{i,j}, y_{i,j}, z_{i,j})$ of the (i, j)th control point in three-dimensional physical space:

$$\mathbf{X}(u, v) = \frac{\sum_{i=0}^{I_{\mathrm{mx}}} \sum_{j=0}^{J_{\mathrm{mx}}} h_{i,j} \mathbf{P}_{i,j} N_{i,k}(u) N_{j,l}(v)}{h} \tag{26}$$

where I_{mx} and J_{mx} denote maximum indices of control points in the i and j directions, respectively, and k and l represent the order of the blending function N used in each direction [25]. Homogeneous coordinates $h_{i,j}$ play a role of weighting factor for each control point. As the value of $h_{i,j}$ increases, the corresponding B-spline curve is closer to the control point. In the present approximation, all the homogeneous coordinates are set to 1.0 to impose equal weighting for each control point. Also, the blending functions are defined as

$$N_{i,k}(u) = \frac{(u - t_i) N_{i,k-1}(u)}{t_{i+k} - t_i} + \frac{(t_{i+k+1} - u) N_{i+1,k-1}(u)}{t_{i+k+1} - t_{i+1}},$$
$$N_{i,0}(u) = \begin{cases} 1 & (t_i \le u \le t_{i+1}) \\ 0 & (\text{otherwise}) \end{cases} \tag{27}$$

where t_i $(i = 0, 1, 2 \cdots)$ are knot-values. The function h, introduced to normalize the local coordinate vector $\mathbf{X}(u, v)$, is defined by

$$h = \sum_{j=0}^{J_{\mathrm{mx}}} \sum_{i=0}^{I_{\mathrm{mx}}} h_{i,j} N_{i,k}(u) N_{j,l}(v) \tag{28}$$

In this process, control points and homogeneous coordinates (weighting factors) are used as design variables. Therefore, the analytic grid sensitivity for surface meshes can be finally evaluated as follows.

For the (i, j)th control point,

$$\frac{\partial \mathbf{X}(u, v)}{\partial \mathbf{P}_{i,j}} = \frac{h_{i,j} N_{i,k}(u) N_{j,l}(v)}{\sum_{q=0}^{I_{\mathrm{mx}}} \sum_{r=0}^{J_{\mathrm{mx}}} h_{q,r} N_{q,k}(u) N_{r,l}(v)} \tag{29}$$

and for the (i, j)th weighting factor,

$$\frac{\partial \mathbf{X}(u, v)}{\partial h_{i,j}} = \frac{N_{i,k}(u) N_{j,l}(v) [\sum_{q=0}^{I_{\mathrm{mx}}} \sum_{r=0}^{J_{\mathrm{mx}}} \{(\mathbf{P}_{i,j} - \mathbf{P}_{q,r}) h_{q,r} N_{q,k}(u) N_{r,l}(v)\}]}{[\sum_{q=0}^{I_{\mathrm{mx}}} \sum_{r=0}^{J_{\mathrm{mx}}} h_{q,r} N_{q,k}(u) N_{r,l}(v)]^2} \tag{30}$$

Consequently, volume grids of each overset mesh block can be modified by mapping from the physical space to u-v plane on the B-spline patch. The grid sensitivities for the volume grids are readily obtained by analytically differentiating algebraic functions in a similar fashion as above, because the sensitivities of real grids are represented by spline functions, weighting factor, and control points. Figure 9 shows the spline patch for a surface at duct entrance and the deformation of overset grid according to the surface change, where dotted points on surface grids indicate control points. If the optimizer relocates the control points, the deformation of surface mesh and their mesh sensitivities can be evaluated according to the deformation of the spline patch. The figure shows that the present approach allows a very high degree of freedom for geometric changes in the design space.

For the present design study, the spline patch is defined by setting where $I_{\mathrm{mx}} = 52$ and $J_{\mathrm{mx}} = 9$, and it is applied to the region of $-1.8 \le x/D_2 \le 0.5$. It is noted that geometric modification is concentrated mostly on upstream of the inlet entrance; the results as demonstrated later will justify this decision.

E. Performance Coefficients

The performance of an inlet is measured by total pressure recovery ratio and engine face distortion. Total pressure recovery ratio, as shown in Eq. (31), is defined by the ratio of average total pressures at AIP to the freestream value at the inflow condition:

$$\eta = \bar{P}_{t,\mathrm{AIP}} / \bar{P}_{t,\mathrm{in}} \tag{31}$$

where $\bar{P}_t$ denotes the average total pressure on each station at AIP and inflow condition.

The inlet distortion in this design work is described by the Society of Automotive Engineers circumferential distortion descriptor DPCP which is defined in the Aerospace Recommended Practice 1420 standard [26,27]. During the design process, the objectives are to

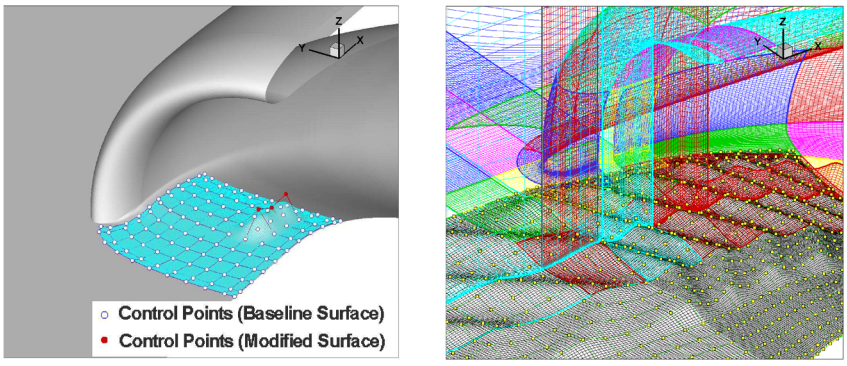

Fig. 9 Spline patch for duct surface (left, conceptual view) and a sample surface shape resulting from the B-spline representation, along with partial surface and volume grids (right).

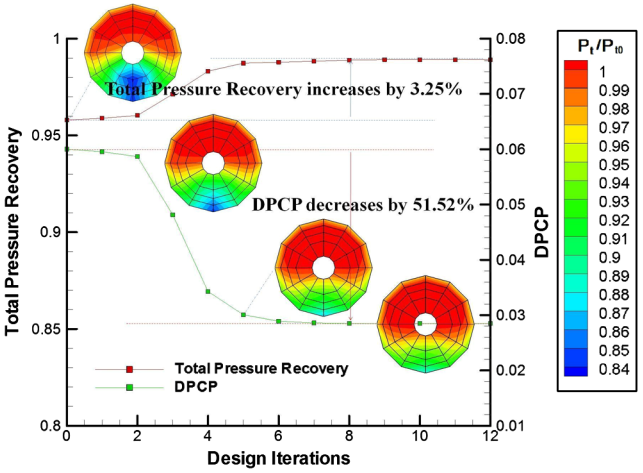

Fig. 10 Design history in terms of total pressure recovery and comparison of total pressure contours at AIP.

diminish engine face distortion and to increase total pressure recovery under the same mass flow rate condition:

$$\mathrm{DPCP}_{\mathrm{avg}} = \frac{1}{N_{\mathrm{rings}}} \sum_{i=1,5} [(P_{t_{\mathrm{avg},i}} - P_{t,\mathrm{low}_{\mathrm{avg},i}})/P_{t_{\mathrm{avg},i}}] \tag{32}$$

where i is the ring number on the AIP rake, N_{rings} is the total number of rings, $P_{t_{\mathrm{avg},i}}$ is the average total pressure of ring i, and $P_{t,\mathrm{low}_{\mathrm{avg},i}}$ is the area average of the low total pressure in region where P_t is below $P_{t_{\mathrm{avg},i}}$. As seen in Eq. (32), DPCP is a measure of uniformity in total pressure over the cross-section sampled by five rings.

F. Design Optimization

The computational cost, an important factor for choosing an optimization technique, in general increases with the number of design variables and complexity (nonlinear characteristics) in the design problem. For flexible modification of the duct geometry, it is necessary to allow a large number of design variables. Adjoint method is employed to conduct the sensitivity analysis for design optimization because its computational cost is relatively insensitive to the size of design variables. To optimize the inlet shape, the surface in the entrance region is modified by adjusting the curvature to meet the design objective. Control points for the B-spline surface are used as the design parameters. Once having obtained the sensitivity vector, we employ the Broyden-Fletcher–Goldfarb–Shanno (BFGS) unconstrained gradient optimization method to find the optimal geometry.

The design problem for the present work is formulated as

$$\text{Minimize} \quad \mathrm{DPCP}_{\mathrm{avg}} \tag{33}$$

$$\text{Subject to} \quad |z_i| \le z_L \qquad (i = 1, 2, \cdots) \tag{34}$$

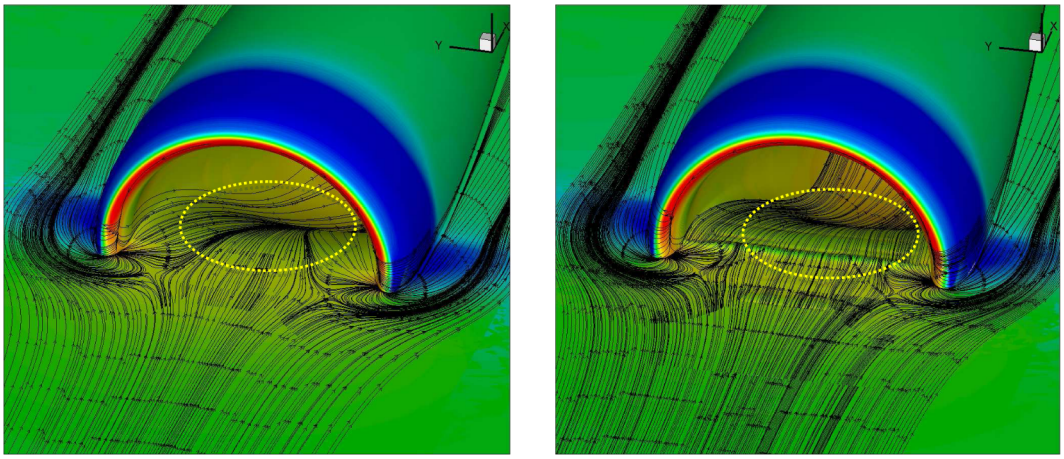

Fig. 11 Comparison of external flow pattern (left, baseline; right, optimal design).

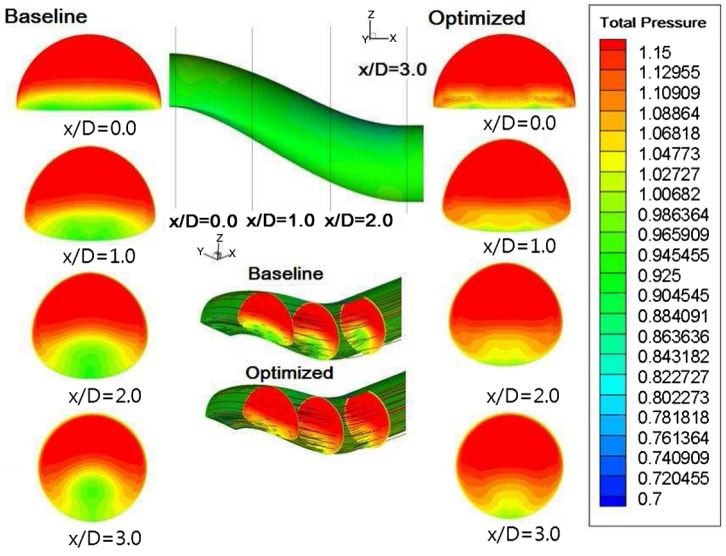

Fig. 12 Comparison of internal flow pattern and total pressure contours at various streamwise locations.

where z_i represents the z coordinate of the ith design variable and z_L denotes the limit of design variables, which is set to be 10% of the height of inlet highlight. In the present shape modification, a total of 468 design variables are used. Figure 10 shows the design history and the evolution of total pressure contours at AIP during the design iterations; clearly, the quality of flow at the engine fan face has been considerably improved. The design iterations are based on the number of sensitivity analysis. The optimal solution at each design step is found by using a cubic function. Thus, more than four iterations of flow analyses are conducted in one design iteration. The total pressure contours at each design iteration show that the improvement of performance comes not only from distortion but also from total pressure. Figure 11 shows how the surface change makes the incoming flow different from that of baseline model; it is observed that a wavy surface in the designed domain is generated through the optimization process and reaches 5% of highlight height at the peak, which is much smaller than the incoming boundary thickness. For the baseline model, the separated flow occurring near the juncture of cowl lip and bottom surface continues to expand laterally, resulting in a significant flow variation (distortion) in the lateral direction at each longitudinal section. On the other hand, the most striking impact on the inlet flow made by the design optimization is that the flow streamlines near the center of the bottom inlet surface are now nearly parallel to the inlet walls; i.e., flow is more uniform in the lateral direction. The separated region near the cowl lip is also reduced, as manifested by the shift of the saddle point towards the lip juncture. A comparison of total pressure contours at various longitudinal stations is shown in Fig. 12. The following is clear in the new design results:

1) The boundary or low-momentum layer (as manifested by low total pressure) is considerably thinner and more uniformly distributed in the lateral direction.

2) The level of total pressure is higher over a larger portion of the inlet duct, indicating that the low-momentum flow at the bottom wall is energized by the wavy surface of the optimized inlet.

As a result of this change of flow pattern, DPCP is decreased by 52.5% from 0.05956 to 0.028492. In addition, the total pressure recovery increases by 3.25% from 0.9589 to 0.9891. Thus, it is concluded that the design process has significantly reduced flow distortion and improved total pressure recovery in the original BLI inlet.

To further evaluate the performance of the new design at various off-design operating conditions as characterized by the area ratio A_0/A_c(=MFR), the total pressure recovery and distortion coefficient are shown in Fig. 13 and compared with those of the baseline model.

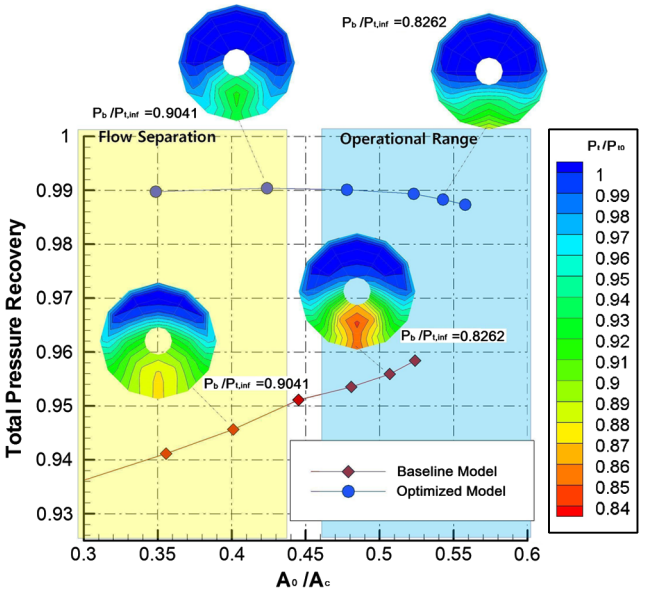

Fig. 13 Comparison of total pressure recovery according to A_0/A_c.

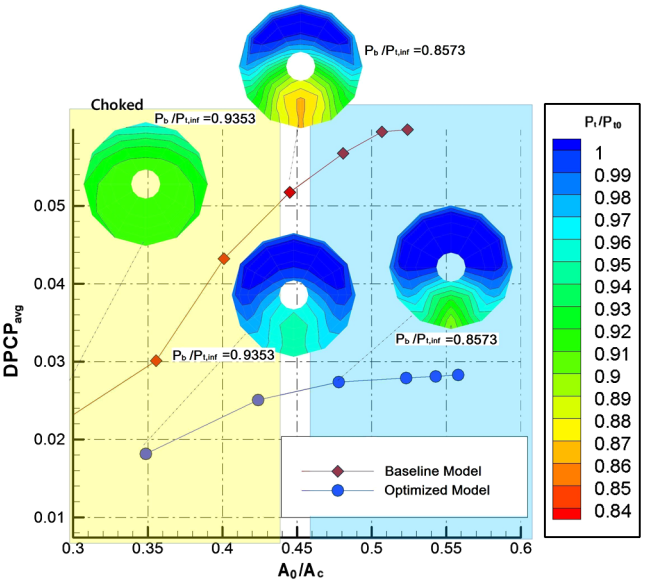

Fig. 14 Comparison of $\mathrm{DPCP}_{\mathrm{avg}}$ according to A_0/A_c.

This area ratio can be adjusted by varying back pressure. As the MFR decreases, the new design still maintains the total pressure recovery constant at 99% for a large range of MFR and only degrades slightly at high A_0/A_c, On the other hand, the total pressure recovery of the baseline model is much lower at low MFR values than that of the new design; the differences between them decreases gradually at higher values of MFR. In Fig. 14, DPCP shows similar trend. The designed model consistently gives a better than 50% reduction in distortion at all conditions and the improvement increases as A_0/A_c increases. It is noted that in both Figs. 13 and 14, the marked points on the curves are obtained, respectively, with the same imposed back pressures for both designs, which results in different area ratios. This suggests that the new design allows more mass flow with larger stream-tube area A_0, to enter the engine for the same back pressure condition. This is consistent with the above observation that the new design produces a flow of more uniform streamlines, higher momentum, and less blockage. This fact is seen clearly in the U-velocity contours at the symmetric plane, as displayed in Fig. 15. The low-momentum layer at the bottom wall due to the flow separation near the lip juncture has been considerably reduced in size and increased in velocity magnitude, resulting in less loss in total pressure throughout the entire inlet. Finally, the oil flow patterns in Fig. 16 again confirm that the new design produces a more uniform flow than the baseline inlet at off-design conditions.

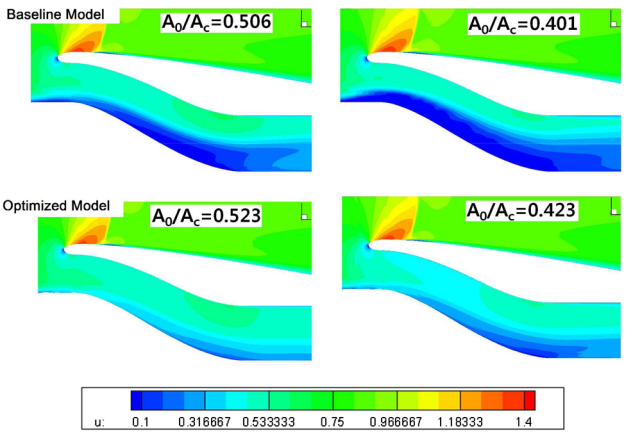

Fig. 15 Comparison of U-velocity contour at symmetric plane for off-design conditions (top, baseline; bottom, optimal design).

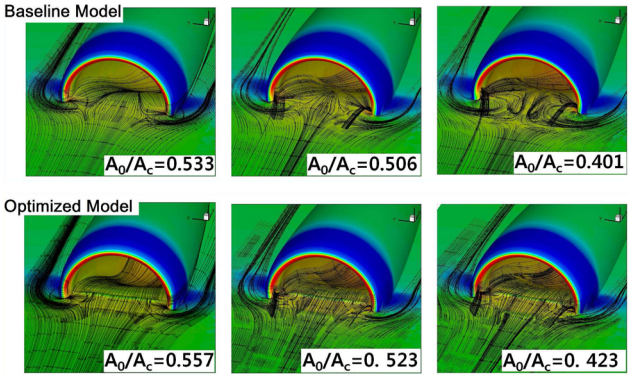

Fig. 16 Comparison of external flow patterns for off-design conditions (top, baseline; bottom, optimal design).

IV. Conclusions

In a BLI inlet, a large amount of boundary-layer ingestion and flow separation at the juncture of cowl lip and bottom surface together can cause significantly high distortion and high total pressure loss. The goal of this study is to minimize these adverse effects on the inlet performance via an automatic and mathematically formulated optimization procedure and a reliable aerodynamic prediction code. The evaluation of aerodynamic performance is based on the high-fidelity k-ω-SST, Navier–Stokes equations solved on an overset mesh system for handling the complex topology of the inlet. In the present design work, the bottom surface geometry of an BLI inlet is altered to maximize its aerodynamic performance, specifically minimizing the total pressure distortion at AIP. The B-spline function is used to describe the geometry of a patch on the bottom surface near the cowl lip with a large number of control points to cover an extended design space. The discrete adjoint method is applied to carry out the sensitivity analysis. To obtain a stable convergence in sensitivity analysis, a numerical dissipation term is added to enhance diagonal dominance of the adjoint matrix. Consequently, the inlet distortion is significantly reduced and the total pressure recovery significantly increased from the baseline model, respectively, by 52.5 and 3.25%. Moreover, the same level of performance also carries over to the off-design conditions.

Acknowledgments

This work is supported under the Subsonic Fixed Wing project of NASA's Fundament Aeronautics Program; William Haller is the Associate Project Investigator. David Arend supplied the baseline geometry file. We thank Theo Theofanous, University of California at Santa Barbara, for making available the computing facility at the Center for Risk Studies and Safety during the course of this study.

References

[1] Daggett, D. L., Kawai, R., and Friedman, D., "Blended Wing Body Systems Studies: Boundary Layer Ingestion Inlets with Active Flow Control," NASA CR-2003-212670, 2003.

[2] Carter, M. B., Campbell, R. L., Pendergraft, O. C., Friedman, D. M., and Serrano, L., "Designing and Testing a Blended Wing Body with Boundary-Layer Ingestion Nacelles," *Journal of Aircraft*, Vol. 43, No. 5, 2006, pp. 1479,1489. doi: 10.2514/1.22765

[3] Kawai, R. T., Friedman, D. M., and Serrano, L., "Blended Wing Body Boundary Layer Ingestion Inlet Configuration and System Studies," NASA CR-2006-214534, 2006.

[4] Taylor, H. D., "Application of Vortex Generator Mixing Principle to Diffusers. Concluding Report," United Aircraft Corp. Research Dept., Rept. R-15064-5, East Hartford, CT, Dec. 1948.

[5] Kaldschmidt, G., Syltedo, B. E., and Ting, C. T., "727 Airplane Center Duct Inlet Low-Speed Performance Confirmation Model Test for Refanned JT8D Engines: Phase 2," NASA CR-134534, Nov. 1973.

[6] Grose, R. M., and Taylor, H. D., "Theoretical and Experimental Investigation of Various Types of Vortex Generators," United Aircraft Corp. Research Dept., Rep. R-15362-5, East Hartford, CT, March 1954.

[7] Anderson, B. H., and Gibb, J., "Vortex-Generator Installation Studies on Steady-State and Dynamic Distortion," *Journal of Aircraft*, Vol. 35, No. 4, 1998, pp. 513–520. doi:10.2514/2.2340

[8] Zhang, W., Knight, D. D., and Smith, D., "Automated Design of a Three-Dimensional Subsonic Diffuser," *Journal of Propulsion and Power*, Vol. 16, No. 6, 2000, pp. 1132, 1140. doi: 10.2514/2.5688

[9] Jirasek, A., "Development and Application of Design Strategy for Design of Vortex Generator Flow Control in Inlets," AIAA Paper 2006-1050, Jan. 2006.

[10] Lim, S., and Choi, H., "Optimal Shape Design of a Two-Dimensional Asymmetric Diffuser in Turbulent Flow," *AIAA Journal*, Vol. 42, No. 6, 2004, pp. 1154, 1169. doi: 10.2514/1.3234

[11] Lee, B. J., and Kim, C., "Automatic Design Methodology of Turbulent Internal Flow Using Discrete Adjoint Formulation," *Journal of Aerospace Science and Technology*, Vol. 11, Nos. 2–3, 2007, pp. 163–173. doi:10.1016/j.ast.2006.12.001

[12] Anabtawi, A. J., Blackwelder, R. F., Lissaman, P. B. S., and Liebeck, R. H., "An Experimental Investigation of Boundary Layer Ingestion in a Diffusing S-Duct with and Without Passive Flow Control," AIAA Paper 99-0739, Jan. 1999.

[13] Gorton, S. A., Owens, L. R., Jenkins, L. N., Allan, B. G., and Schuster, E. P., "Active Flow Control on a Boundary-Layer-Ingesting Inlet," AIAA Paper 2004-1203, Jan. 2004.

[14] Berrier, B. L., and Allan, B. G., "Experimental and Computational Evaluation of Flush-Mounted, S-Duct Inlets," AIAA Paper 2004-1203, Jan. 2004.

[15] Allan, B. G., Owens, L. R., and Berrier, B. L., "Numerical Modeling of Active Flow Control in a Boundary Layer Ingesting Offset Inlet," AIAA Paper 2004-2318, June 2004.

[16] Allan, B. G., Owens, L. R., and Lin, J. C., "Optimal Design of Passive Flow Control for a Boundary-Layer-Ingesting Offset Inlet Using Design-of-Experiments," AIAA Paper 2006-1049, Jan. 2006.

[17] Berrier, B. L., Carter, M. B., and Allan, B. G., "High Reynolds Number Investigation of a Flush-Mounted, S-Duct Inlet with Large Amount of Boundary Layer Ingestion," NASA TO-2005-213766, 2005.

[18] Chung, J. K., and Cole, G. L., "Comparison of Compressor Face Boundary Conditions for Unsteady CFD Simulations of Supersonic Inlets," AIAA Paper 95-2627, July 1995.

[19] Owens, L. R., Allan, B. G., and Gorton, S. A., "Boundary-Layer-Ingesting Inlet Flow Control," AIAA Paper 2006-0839, 2006.

[20] Menter, F. R., "Two-Equation Eddy-Viscosity Turbulence Models for Engineering Applications," *AIAA Journal*, Vol. 32, No. 8, 1994, pp. 1598, 1605. doi: 10.2514/3.12149

[21] Kim, S., Kim, C., Rho, O., and Hong, S., "Cures for the Shock Instability: Development of Shock-Stable Roe Scheme," *Journal of Computational Physics*, Vol. 182, No. 2, 2003, pp. 342, 374. doi:10.1016/S0021-9991(02)00037-2

[22] Yoon, S., and Jameson, A., "Lower-Upper Symmetric-Gauss–Seidel Method for the Euler and Navier–Stokes Equation," *AIAA Journal*, Vol. 26, No. 9, 1988, pp 1025, 1026. doi: 10.2514/3.10007

[23] Lee, B. J., and Kim, C., "Aerodynamic Redesign Using Discrete Adjoint Approach on Overset Mesh System," *Journal of Aircraft*, Vol. 45, No. 5, 2008, pp. 1643, 1653. doi: 10.2514/1.34112

[24] Koc, S., Nakahashi, K., and Kim, H., "Aerodynamic Design of Complex Configurations with Junctions," *Journal of Aircraft*, Vol. 43, No. 6, 2006, pp. 1838, 1844. doi: 10.2514/1.20723

[25] Lee, B. J., "Aerodynamic Shape Optimization for Internal and External Flows via Discrete Adjoint Approach and Overset Mesh System," Ph.D. Dissertation, Seoul National Univ., School of Mechanical and Aerospace Engineering, 2007.

[26] "Gas Turbine Engine Inlet Flow Distortion," Society of Automotive Engineers, Rept. ARP-1420, March 1978.

[27] Anderson, B. H., and Keller, D. J., "Considerations in the Measurement of Inlet Distortion for High Cycle Fatigue in Compact Inlet Diffusers," NASA TM-2002-211476, 2002.

[28] Hicks, R. M., and Henne, P. A., "Wing Design by Numerical Optimization," *Journal of Aircraft*, Vol. 15, No. 7, 1978, pp. 407, 412. doi: 10.2514/3.58379

T. Zang
Associate Editor